Research Article

ADVANCED PHOTONICS

Blob detection for photonic metasurface designing: angular and spectral control of scattered light

Anja Tiede,[a,b] **Nick Feldman**,[b,c] **Alexander Lambertz**,[b,d] **A. Femius Koenderink**,[b,d] **Anna Fontcuberta i Morral**,[a,e] **and Esther Alarcon-Llado**[b,f,*]

[a]École Polytéchnique Fédérale de Lausanne, Institute of Materials, Laboratory of Semiconductor Materials, Lausanne, Switzerland
[b]NWO-Institute AMOLF, LMPV-Sustainable Energy Materials, Amsterdam, The Netherlands
[c]Advanced Research Center for Nanolithography, Amsterdam, The Netherlands
[d]University of Amsterdam, Institute of Physics, Amsterdam, The Netherlands
[e]École Polytéchnique Fédérale de Lausanne, Institute of Physics, Lausanne, Switzerland
[f]University of Amsterdam, Van 't Hoff Institute for Molecular Sciences (HIMS), Amsterdam, The Netherlands

Abstract. Metasurfaces with precise spectral and angular control of light scattering are of growing interest for photonic applications requiring advanced photon management. Correlated disorder emerged as a promising route for angular control of light scattering, but most design approaches are computationally expensive or do not allow spectral tunability. Here, we introduce an inverse design approach for correlated-disordered metasurfaces based on tailoring the Fourier space and blob detection to create point distributions that are later "decorated" with individually designed nano-resonators or meta-atoms to tune the optical response for the desired functionality. We validate the control of the angular scattering by fabricating ensembles of Au nano-pillars following our design and characterizing their angular scattering with Fourier microscopy. We expand the limits of our versatile approach by combining multiple metasurfaces in one, effectively adding their individual scattering characteristics. Moreover, we demonstrate how the choice of decorative unit tunes the spectral response. In summary, we can address spectral and angular ranges independently, yielding a high degree of control of the scattering response.

Keywords: metasurface; inverse design; superposition; Fourier microscopy.

Received Jul. 16, 2025; revised manuscript received Feb. 18, 2026; accepted for publication Apr. 24, 2026; published online May 25, 2026.

[DOI: 10.1117/1.AP.8.3.036005]

1 Introduction

Metasurfaces have garnered significant attention because they can manipulate light scattering across a broad angular and spectral range.[1–4] Moreover, metasurfaces composed of meta-atoms arranged in a periodic structure enable arbitrary wavefront shaping as the individual meta-atom can be chosen to adapt the ensemble's response for different functionalities.[5–8] Particularly, metasurfaces with a certain degree of disorder offer enhanced broadband light trapping capabilities because of their optimized k-space, making them highly effective for thin-film solar cells.[9–14] Typical design procedures for these light-trapping structures include iterative inverse design approaches or other numerical optimization schemes to solve a prescribed objective.[10,11,13,14] Although recent reports have expanded to include machine-learning-based and neural network-assisted design approaches, these remain computationally intensive.[15,16]

A more elegant solution is to design metasurfaces directly in k-space using a one-dimensional (1D) representation function, the spectral density function (SDF), resulting in interconnected channel-type structures.[11,12] The SDF is the radially averaged power spectral density. It represents the structure in reciprocal space and characterizes its light–matter interaction because of the relation between Fourier space and far-field scattering.

*Address all correspondence to Esther Alarcon-Llado, e.alarconllado@amolf.nl

This concept has been widely utilized to obtain light trapping patterns for solar cells using either iteration-based routines (optimization[10,13,14] and simulated annealing[17]), naturally occurring spinodal decomposition processes,[12,18] or design-based techniques.[9,11] Unfortunately, each approach yields interconnected channel-type structures that are limited in design variability because they do not support the incorporation of meta-atoms, i.e., isolated decoration units with individually tunable resonant responses, by, for example, varying their size or shape.[19–22] Exploiting this can enable multi-resonant responses, desirable, e.g., for enhancing light coupling in thin-film solar cells.[23,24] Various k-space engineering approaches have been proposed to design isolated structures with a determined k-space, for example, using random sphere packing[11] or molecular-dynamics-simulated annealing procedures.[25] However, these methods offer limited flexibility in designing the individual decoration unit and/or rely on computationally expensive iterative routines.

This paper introduces and experimentally demonstrates an efficient design approach to generating a metasurface consisting of scattering units distributed in a pattern with a targeted k-space. To the best of our knowledge, this work represents the first demonstration of combining blob detection, an image analysis concept, with k-space engineering to identify locations with targeted spatial correlation. A second step is to re-decorate the points with individual scattering units. This approach allows flexible tunability through designing the scattering units: tailoring resonances in the decoration units can engineer the spectral response, and the correlation in the spatial distribution of the scatterers determines the angular scattering of light. We show that it is also possible to design more complex angular and spectral scattering properties: by interlacing different basic elements into a single metasurface, one can obtain a scattering response that is the sum of the responses of the two basic structures. Taking these qualities together, our proposed approach provides a highly flexible toolbox to design photonic metasurfaces.

2 Materials and Methods

2.1 Input and Output Patterns Representation

This work uses the SDF to characterize the real-space patterns, a concept readily employed in microstructure analysis and photonic design.[11,12,26–28] The 1D SDF is the normalized azimuthally averaged magnitude square of the Fourier spectrum of a real space structure $Z(\mathbf{r})$,

$$F\{Z(\mathbf{r})\}(\mathbf{k}) = A_\mathbf{k} \cdot e^{i\phi_\mathbf{k}},$$
$$f_{\mathrm{SDF}}(\mathbf{k}) = (A_\mathbf{k})^2/C, \tag{1}$$

where $A_\mathbf{k}$ and $\phi_\mathbf{k}$ are the magnitude and phase values at each point $\mathbf{k}$, respectively, in reciprocal space, and C is the normalization constant to ensure comparability in the representation, chosen as the maximum of $A_\mathbf{k}^2$ over the range of interest. We only consider in-plane isotropic diffraction; thus, $f_{\mathrm{SDF}}(\mathbf{k})$ can be reduced to a 1D scalar representation $f_{\mathrm{SDF}}(k)$ of the 2D Fourier space. The SDF contains information on structural correlations in the real-space pattern. This is similar to, e.g., X-ray diffraction, where the far-field diffraction pattern reveals the structure factor, i.e., the Fourier transform of the real-space pattern at hand. Moreover, the SDF characterizes the angle-dependent light scattering of the metasurface, and therefore, we use it as input for the design routine. From this, we generate a point pattern and assign a decoration unit to each point (see Sec. 2.2), creating a real space pattern with isolated unit cells that contains most of the structural correlations of the input design. In the first Born approximation (i.e., the limit of single scattering that applies to low index-contrast structures), this corresponds to evaluating the product of the structure factor (i.e., the Fourier transform of the lattice geometry) and the form factor (i.e., the single unit cell scattering function approximated as the Fourier transform of the geometry).

2.2 Point Pattern Generation with Blob Detection on Correlated Gaussian Random Fields

From the input SDF, we generate binary patterns using the Gaussian random field (GRF), also known as the spinodal approach.[11,12,29,30] To construct the (complex) Fourier space from the 1D SDF, we assign each point an amplitude $A_\mathbf{k}$ proportional to the corresponding point on the SDF, and a random phase $\phi_\mathbf{k}$ uniformly distributed in the range $[-\pi, \pi)$. The real-space Gaussian random field $\Phi(\mathbf{r})$ is obtained via an inverse Fourier transform; pixel values in $\Phi(\mathbf{r})$ follow a Gaussian distribution. Many works use the GRF-generated real-space function $[\Phi(\mathbf{r})]$ to obtain a binary pattern by thresholding $\Phi(\mathbf{r})$ with a defined cutoff value (Φ_0) so that all positions $\mathbf{r}$ with $\Phi(\mathbf{r}) < \Phi_0$ are assigned to one material and those where $\Phi(\mathbf{r}) > \Phi_0$ are assigned to the second material. Φ_0 is a value chosen to yield a desired filling fraction. Thresholding yields a spinodal binary pattern with interconnected features where only minor spatial correlations are lost compared with $\Phi(\mathbf{r})$.

Instead of thresholding, in this work, we transform the real-space function $\Phi(\mathbf{r})$ to generate a point pattern with isolated structures using blob detection. In image analysis, a "blob" is defined as a region in an image that visually differs from its local surroundings.[31,32] Blob detection is an established method in image processing that has found its way into disciplines from medicine (e.g., to identify caries[33] or cancer)[34] to physics (e.g., to identify atomic columns in transmission electron microscopy images[35]). Specifically, we use the Laplacian of Gaussians variant from the scikit-image Python library because of its higher read-out accuracy[36] to identify a set of coordinates with similar spatial correlations as in $\Phi(\mathbf{r})$. Full implementation details are provided in the Supplementary Material.

2.3 Au Nano-Pillar Fabrication

To experimentally demonstrate our concept, we fabricate and characterize metasurfaces designed with Au nano-pillars as scatterers, owing to their strong resonant scattering that can be tuned via the Au nano-pillar dimensions. Au nano-pillar metasurfaces were fabricated on a silicon substrate using e-beam lithography (Raith EBPG5000, Dortmund, Germany) and methyl methacrylate/poly(methyl methacrylate) (MMA/PMMA)-positive resist, followed by evaporation and lift-off. The size of each pattern was 2 mm × 2 mm, realized by repeating a 50 μm × 50 μm unit cell; ~300-nm-thick Au was evaporated on top of a 10-nm Ti wetting layer (Leybold Optics Lab 600H, Alzenau, Germany), followed by lift-off in acetone. The pillar height was confirmed using atomic force microscopy (Bruker FastScan AFM, Camarillo, California, United States, see Supplementary Material). The actual diameters of the pillars differ from the input design dimensions due to the exposure conditions and were confirmed by scanning electron microscopy (SEM) (Zeiss Merlin, EHT 3.0 kV, Oberkochen, Germany) and atomic force microscopy. No differences in pillar geometries were found between the center and edge of the pattern.

2.4 Fourier Microscopy

We use Fourier microscopy in reflection mode to identify the angular-dependent scattering response of the patterns. Fourier microscopy allows us to measure the angular dependence of light scattering by imaging on the back focal plane.[37] The principle is described in more detail in Refs. 38–40. We illuminate our samples with a supercontinuum laser (NKT Whitelase Micro, Copenhagen, Denmark) coupled to a single-mode optical fiber (Thorlabs P1-630A-FC-5, single-mode patch cable, 633 to 780 nm, Newton, New Jersey, United States) and collimated to a Gaussian beam. The illumination wavelength is selected with a 10-nm band-pass filter centered around 640 nm (Thorlabs), and the total power of the nominally unpolarized light is 1.145 μW. The scattered light is captured by the objective (NA = 0.95) and then imaged onto a CMOS camera (Basler, acA1920-40um, Ahrensburg, Germany) using a relay lens setup. Each image is taken with a 20-ms integration time. A beam block placed in the conjugate Fourier plane of the objective reduces the influence of the directly reflected light from the sample in the image. The radially averaged scattering profiles are obtained by azimuthal averaging of the measured Fourier-plane intensity and normalized to their maximum. The origin for the radial k-space profile was set by identifying the center of the objective's back focal plane within the recorded image.

2.5 Electromagnetic Simulations

To complement our study on plasmonic realizations, we also explore dielectric nano-scatterer point patterns. To that end, we implement a calculation workflow in which far-field light scattering and forward scattering cross-sections were calculated using a commercial finite-difference time-domain (FDTD) solver.[41] The patterns are considered a dielectric with $n = 3.5$ and a height of $h = 200$ nm on a lossless, dispersion-less substrate of the same dielectric. For the far-field light scattering calculations, the simulation size was $10\ \mu m \times 10\ \mu m \times 0.38\ \mu m$, with a minimum mesh step size of 6 nm using automatic non-uniform meshing, and a refined mesh of 2 nm around the pattern. Periodic boundary conditions were implemented in the x and y directions and perfectly matched layers in the z direction. To quantify the power scattered per unit angle, incident power, and photon energy, the far-field projection is calculated from a transmission monitor 20 nm below the pattern. Due to the high memory requirements of the simulations, they are performed on the Snellius supercomputer cluster (SURF, NL) using CPU computing nodes. Each simulation required up to ~14 h of wall-clock time and up to ~400 GB of memory.

For the scattering cross-section calculations, the simulation size is chosen as 2 μm in all dimensions with a minimum mesh step size of 0.8 nm and using conformal meshing. The total-field-scattered-field source is injected along the z-axis, spans 500 nm in all directions, and covers the wavelength range from 300 to 1100 nm. Field monitors are placed only within the substrate to register the fields scattered into the substrate. We calculate the forward scattering cross-section Q_{scat} by normalizing the transmitted power through the monitor to the source intensity and the geometrical cross-section of the scattering object.

3 Results and Discussion

3.1 Non-Iterative Approach for Generating Correlated-Disordered Point Patterns Using Blob Detection

We introduce a non-iterative inverse-design approach to generate two-dimensional point patterns, which serve as a foundation for metasurfaces with well-defined angular and spectral scattering responses [see Figs. 1(a)–1(c)]. The angular scattering is governed by the correlated-disordered lattice in real space, whereas the spectral response is determined by the geometry of nano-scatterers used to decorate the identified positions in the point pattern.

The correlated-disordered point pattern is generated from the momentum space through a combination of GRF modeling[11,12] and blob detection (see Sec. 2 and Supplementary Material). We use the SDF as a 1D representation of the desired power distribution in the momentum space [black line in Fig. 1(b)] to generate a GRF image in the real space [Fig. 1(a), left]. Although the GRF image contains Gaussian-distributed pixel values, it is evident that there are regions of enhanced spatial correlation that differ from their surroundings, referred to as "blobs" in image

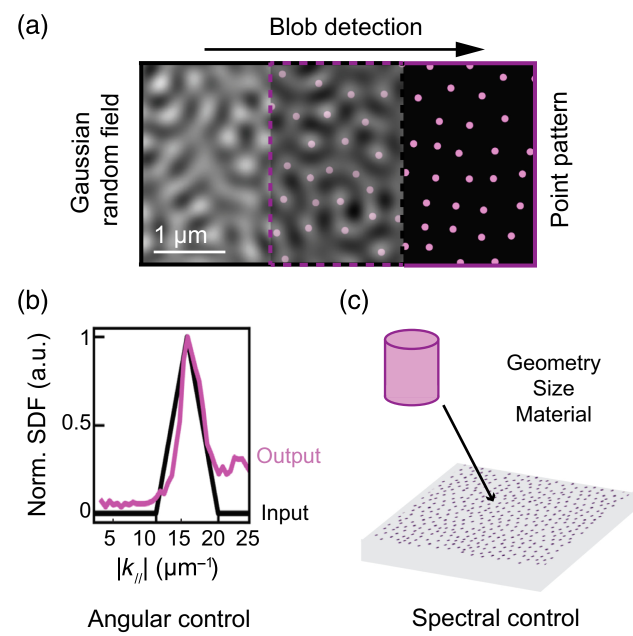

Fig. 1 Metasurface generation using Gaussian random field modeling, blob detection, and nano-resonator decoration. The workflow illustrated here is the conceptual basis for the experimental and computational investigations presented in the subsequent figures. The point pattern provides the angular control of light scattering as highlighted in panels (a) and (b). (a) Correlated Gaussian random field image (left) and point pattern identified by the blob detection algorithm (right). The middle panel shows an overlay of the continuous GRF and the discrete points, illustrating the mapping from field to point pattern. (b) 1D representation function of the Fourier space through the SDF of the input (black line) and extracted from the generated pattern (purple line). (c) Schematic representation of a metasurface obtained by decorating the point pattern with nano-resonators. The nano-resonator's geometry, size, and material control the spectral response.

processing. Identifying them using a blob detection algorithm yields a set of spatial coordinates [Fig. 1(a), right] that preserves most of the targeted spatial correlation given in the input SDF. This is evident by the close match between the SDF of the final pattern (purple line) and the input (black line) in Fig. 1(b).

We further verify this claim by calculating the cosine similarity of the generated SDFs to the input SDF. Although this approach is generally used to determine the similarity of text or documents in natural language processing, machine learning, or artificial intelligence applications, here, we use it to quantify how well the shape of the input SDF is preserved in the generated SDF on a scale from 1 (identical) to 0 (wholly distinct). The input and output SDFs in Fig. 1(b) give a cosine similarity of 0.91, confirming very good shape replication.

This property is true for a wide range of input SDFs, making our approach as versatile as GRF modeling (see Supplementary Material). Moreover, the cosine similarity is only mildly affected (<0.05) by changes in size or resolution of the chosen field. Therefore, our approach scales robustly with system size and notably does not require iterative loops, so it is limited only by available computational memory.

Once the 2D point pattern is generated, we decorate each point in real space with a scattering unit [Fig. 1(c)]. This method is an established approach for the design of metasurfaces with periodic lattices and, more recently, has been extended to hyperuniform correlated-disordered systems.[9,25] Each decoration unit can be modified in geometry, dimensions, or material to tailor the individual response, thereby tuning the ensemble's response.[20–22] The spectral position of the scattering peaks is governed by size-dependent resonant modes of the nano-resonators, with larger dimensions leading to redshifts and smaller dimensions to blueshifts.[19] Similarly, the scattering amplitude scales with resonator volume and depends on the refractive index contrast with the surrounding media.

As the generated SDF is a result of both the generated point distribution and the decoration step, the chosen geometry and dimensions will also affect the similarity of the generated SDF to the input, which we explore in the Supplementary Material. However, in this work, we modify the decoration unit's spectral scattering characteristics to demonstrate that, in our approach, the point pattern generation and the resonator design present two separate parameters that allow angular and spectral control to be tailored separately. The workflow illustrated in Fig. 1 forms the basis for the metasurface realizations presented in this work, which are validated through experimental characterization (Figs. 2 and 3) and complementary computational investigations (Figs. 4 and 5).

3.2 Demonstration of Angular Scattering Control

Having introduced the method, we now experimentally examine the angular scattering of an ensemble of Au nano-pillars placed according to our design approach via Fourier microscopy measurements. Au is selected for the experimental realization due to its high broadband reflectivity, which ensures sufficiently strong scattering signals for reliable Fourier microscopy characterization. To this end, we fabricate two metasurfaces with nano-pillars at the coordinates given by two rectangular input functions: $I_A(k)$ and $I_B(k)$, where $I_A(k)$ peaks between $k \in [4, 6]$ μm^{-1} and $I_B(k)$ between $k \in [7, 8]$ μm^{-1} [see Fig. 2(a)]. Figure 2(b) shows representative excerpts of the resulting point patterns, generated with a total size of 50 μm × 50 μm.

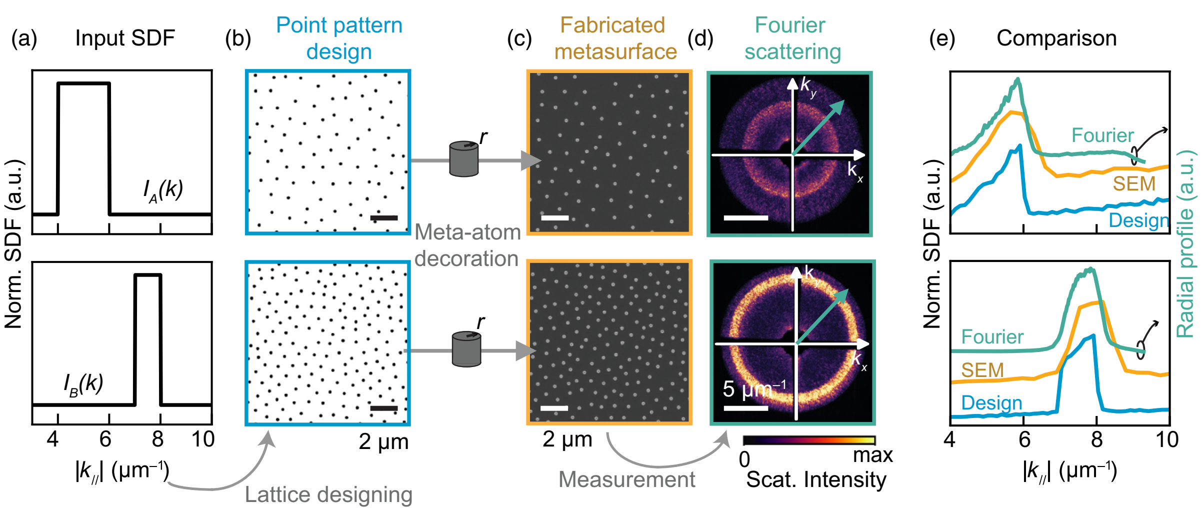

Fig. 2 Experimental demonstration of angular scattering from correlated-disordered metasurfaces using Fourier microscopy. (a) Two rectangular SDF profiles, $I_A(k)$ and $I_B(k)$, are used as input functions. The SDFs have a plateau for $k_A \in [4, 6]$ μm^{-1} and $k_B \in [7, 8]$ μm^{-1}. (b) Representative real space point patterns generated from the input functions in panel (a). Full pattern size: 50 μm × 50 μm. (c) Representative SEM images of the fabricated metasurfaces with Au nano-pillars ($r \sim 130$ nm, $h \sim 300$ nm) on Si. (b) and (c) Excerpts taken from different spatial regions of the same larger pattern. (d) Fourier scattering microscopy images at $\lambda = 640$ nm from each metasurface. The colorbar indicates the scattering intensity, and both measurements are normalized to the common maximum. (e) SDFs of the real space design (blue lines), SEM images (orange lines), and Fourier reflectance images (green lines). The graphs are normalized to the maximum value in the depicted range and shifted on the vertical axis for clarity.

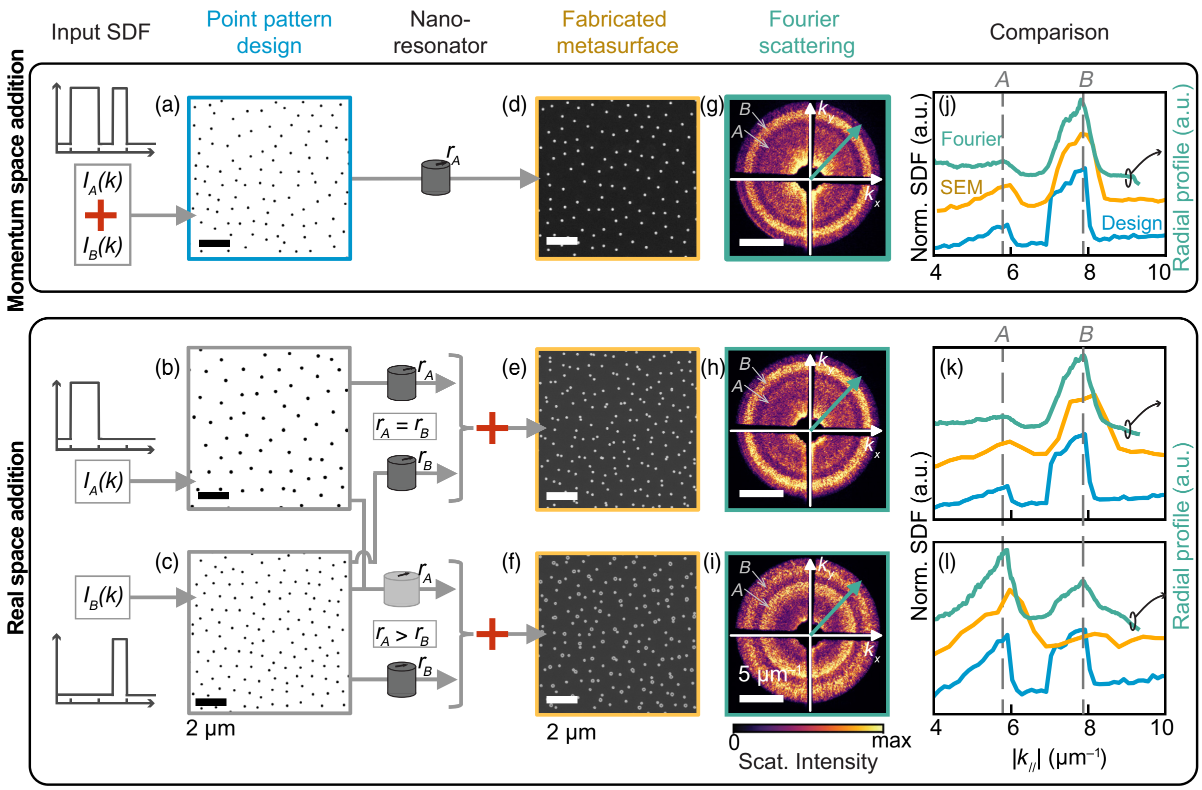

Fig. 3 Generation of new metasurfaces based on the superposition of two patterns, shown using Fourier microscopy. Profile A is defined as a rectangular function with a plateau between $k \in [4, 6]$ µm^{-1}; profile B is defined as a rectangular function with a plateau between $k \in [7, 8]$ µm^{-1}. (a)–(c) Real-space patterns created using our method for the different input profiles. (a) Pattern obtained from an input SDF corresponding to the sum of profiles A and B. (b) and (c) Patterns obtained individually from profile A (b) and profile B (c). For the combined realization in panels (e) and (f), each constituent pattern is decorated with a distinct nano-resonator and then superimposed, as illustrated in the sketch. Here, r_A and r_B denote the nominal radii of the two cylindrical nano-resonator types. (d)–(f) SEM images of fabricated Au pillars on a Si substrate. (g)–(i) Fourier scattering microscopy images of the nano-structures obtained by illumination with unpolarized laser light filtered at $\lambda = 640$ nm with a 10-nm bandwidth. The colorbar indicates the scattering intensity, where each image is normalized to its maximum. (j)–(l) Extracted SDFs of the real space design and the SEM images, compared with the radially averaged profiles extracted from the Fourier microscopy images in panels (g)–(i). The graphs are normalized to the maximum value in the depicted range and shifted vertically for clarity. The vertical guide lines in panels (j)–(l) indicate the SDF peaks corresponding to the highlighted scattering rings marked in panels (g)–(i).

As expected from the input, the point density is higher for input functions with larger spatial frequencies. Figure 2(c) shows representative SEM images of the as-fabricated metasurfaces. In both patterns, the fabricated nano-pillars have diameters of ~260 nm and heights of ~300 nm (see Supplementary Material).

We use Fourier microscopy to characterize the metasurfaces at $\lambda = 640$ nm [see Fig. 2(d)] by illuminating the sample with unpolarized light through normal incidence wide field illumination. Fourier microscopy gives insight into the angular scattering response of the structures in a single measurement by imaging the scattered signal in the back focal plane. The black cross through the center is caused by a beam block that blocks most of the zero-order reflection. Details on the measurement setup can be found in Sec. 2. In both angular scattering patterns, isotropic scattering can be observed as a ring around the center, as expected given the input function and coinciding with that given in quasi-random patterns. As expected, the ring radius is smaller in the metasurface generated from $I_A(k)$ than that generated by $I_B(k)$. It is interesting to note that the metasurface with the higher point density shows a larger scattering strength. Given that the pillars' dimensions are identical in both patterns, we expect that the scattering intensity is modified solely by the density of pillars in each design. To better compare the scattering profile with the input SDF, Fig. 2(e) shows the radially averaged profiles of the Fourier reflectance image (green, see Sec. 2) and SDF of the generated point pattern (blue), as well as the radially averaged Fourier transform of the SEM image (orange). Each curve is normalized to its maximum, and the curves are vertically shifted for clarity. The apparent discrepancy with the rectangular shape of the input SDF [Fig. 2(a)] arises from the design framework itself and is discussed further in the

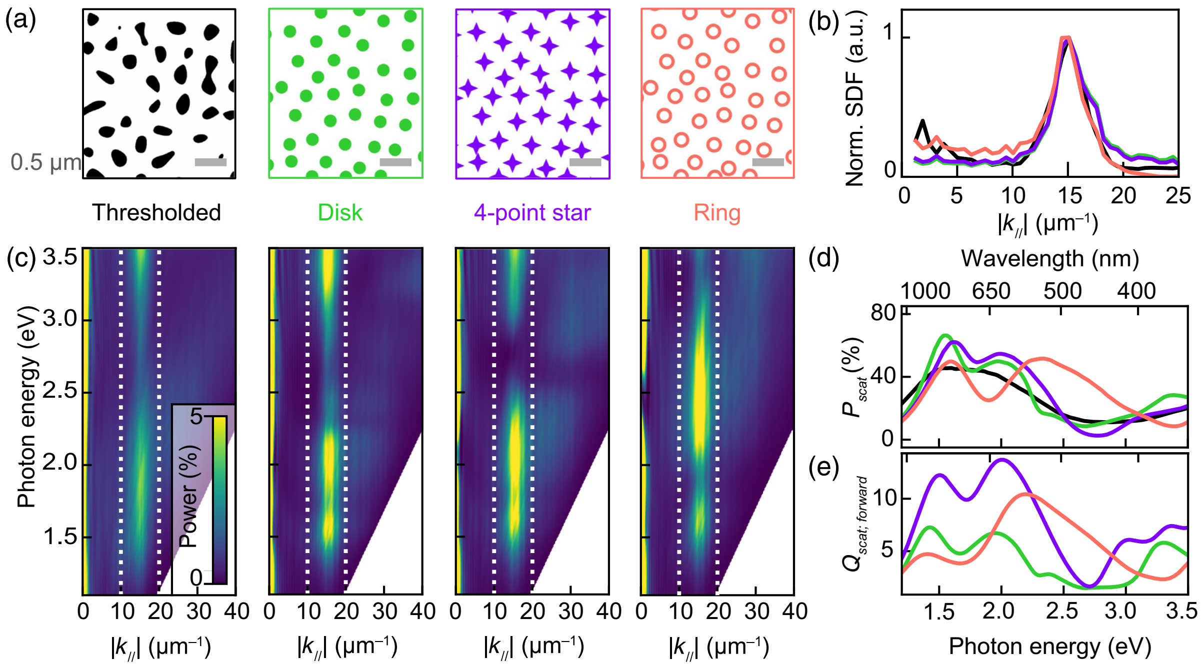

Fig. 4 Comparison of simulated results (FDTD) for scattering into the far-field through a pattern decorated with differently shaped scattering units and forward scattering of each single scattering unit. The same triangular symmetric input function creates four patterns in panel (a): a thresholded version and one set of coordinates for the point patterns. The points are decorated with different shapes, namely, rings (red), circles (green), and stars (purple). The colors serve as the legend for panels (b), (d), and (e). The dimensions of the single resonators and the binary threshold were chosen to maintain a filling fraction of around 16% in the full pattern. (b) SDF of the patterns in panel (a). (c) Angular dependence of the scattering for different patterns calculated from the far-field transformation of the power transmitted through the indicated pattern (dielectric $n = 3.5$, $h = 200$ nm) on a lossless, dispersion-less substrate of the same material. The color represents the fraction of incident power scattered into a specific in-plane momentum range. White dashed lines indicate $k_1 = 10\ \mu\text{m}^{-1}$ and $k_2 = 20\ \mu\text{m}^{-1}$, the region where the scattering of the patterns is designed for. (d) Integrated power scattered into the region of $[k_1, k_2]$. (e) Forward scattering cross-sections of each resonator ($h = 200$ nm, dielectric of $n = 3.5$ placed on a substrate of the same refractive index).

Supplementary Material. Although the three curves are aligned visually in their main features, there are slight differences. The SDF of the SEM image (orange, middle curve) is consistently shifted to higher k-values compared with the pattern design (blue, lower curve), which we attribute to the different resolutions of the images (5 nm/px for the design compared with ~27 nm/px for the SEM image, see Supplementary Material). Despite this offset, the SDF extracted from the SEM image retains the same characteristic shape as the one from the designed point pattern. Furthermore, the radial profiles extracted from the Fourier scattering images match both the shape and position of the designed SDF. Taken together, these observations confirm that the angular scattering response is governed by the correlations in the point distribution designed with our method, as demonstrated experimentally in this subsection.

3.3 Superposition of Metasurface Designs in Real and Momentum Spaces

We now explore how more complex metasurfaces can be generated by superimposing two (or more) independently designed patterns. This strategy enables hybrid designs that combine distinct angular or spectral scattering features within a single device (layer). Under the assumption of linear, non-interacting scattering contributions, metasurface designs can be combined either in the real space (by overlaying spatial patterns) or in the momentum space (by summing their target SDFs). We explore both approaches with the two input functions, $I_A(k)$ and $I_B(k)$, as previously introduced.

For adding patterns in the momentum space (Fig. 3, top row), the combined SDF $I_{A,B}(k) = I_A(k) + I_B(k)$ is used to generate a point pattern subsequently decorated with identical disk-shaped resonators [$r = 80$ nm, Fig. 3(a)]. For adding patterns in the real space (Fig. 3, middle, bottom row), two independent point patterns—derived separately from $I_A(k)$ and $I_B(k)$—are overlaid upon decoration with disks of either equal radii ($r_A = r_B = 80$ nm) or different radii ($r_A = 113$ nm, $r_B = 80$ nm). The independent choice of a nano-resonator for each pattern opens an exciting avenue to target more complex scattering responses. To experimentally validate this concept, we fabricate all metasurface variants as Au nano-pillars on a Si substrate [Figs. 3(d)–3(f)], resulting in radii of ~195 and ~260 nm and a height of ~300 nm (see Supplementary Material). The angular scattering properties are characterized using Fourier scattering

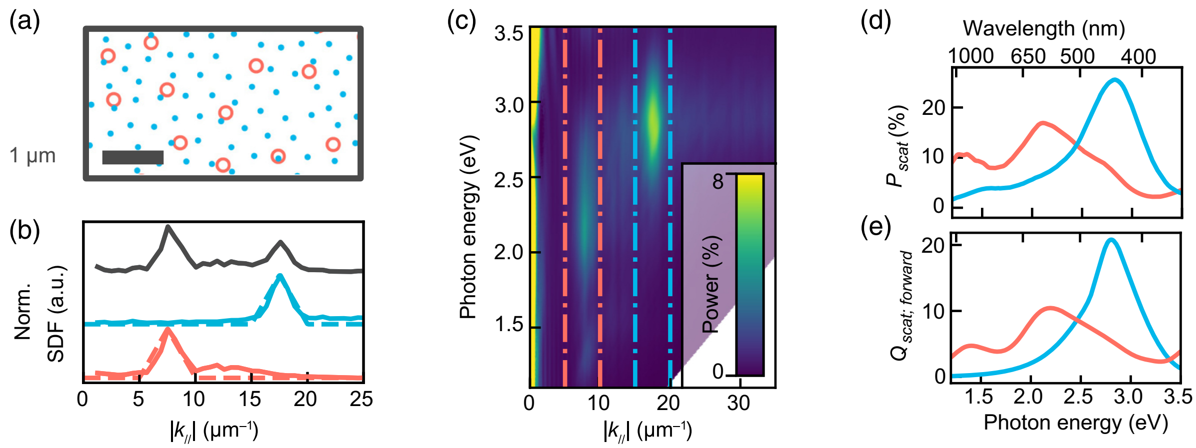

Fig. 5 Far-field scattering for a pattern with different decoration units compared with the forward scattering for each building block, computed by FDTD. (a) Summation of two patterns designed for different scattering ranges. The underlying subpatterns are highlighted in different colors: a point pattern designed for the range of $k \in [5, 10]$ μm^{-1} is decorated with rings ($r_{\text{inner}} = 75$ nm, $r_{\text{outer}} = 125$ nm) and shown in red. Blue is a point pattern for the range of $k \in [15, 20]$ μm^{-1} and decorated with a disk of $r = 50$ nm. The patterns were added in real space into a single plane; the colors are for clarification only. (b) Corresponding SDF from the different patterns. In red (blue), the SDF for the ring (disk) subpattern is given. Each subpattern was created with a triangular input SDF of 5 μm^{-1} width and peak at the center, shown as a dashed line in the same color. The SDF of the pattern generated by real-space addition of the two subpatterns is shown in gray. Each profile is normalized to its maximum, and the patterns are shifted for clarity. (c) Fraction of the incoming power scattered into the far-field for the pattern in panel (a) implemented as dielectric ($n = 3.5$, $h = 200$ nm) on a lossless, dispersion-less substrate of the same refractive index. The dash-dotted lines indicate the range for which each subpattern was designed in the respective color. (d) Integrated power for each subpattern, i.e., the ring subpattern integrated for range $k \in [15, 20]$ μm^{-1} (red) and the disk subpattern integrated for range $k \in [15, 20]$ μm^{-1} (blue). (e) Forward scattering cross-sections of the two different nano-resonators used to generate the pattern (red: ring-shaped; blue: disk-shaped). For color: see online.

microscopy centered at 640 nm wavelength [Figs. 3(g)–3(i)], resulting in double-ring scattering features for each metasurface, consistent with the composite input SDFs. The extracted radially averaged profiles of the Fourier scattering (green), Fourier transform of the SEM images (orange), and the input designs (blue) are shown in Figs. 3(j)–3(l). The strong correspondence among the three different curves for each metasurface confirms the regime of non-interacting structures.

Although both addition approaches produce the expected double-ring profiles, the relative scattering intensities differ. As noted in the previous section, features at larger wavevectors in the input profile lead to a higher density of points in these patterns, resulting in a systematic increase of intensity in the generated SDF as the wavevector increases.[11] This is a direct consequence of our metasurface design method and explains the different intensities between the inner and outer ring radial profiles. The effect becomes particularly evident when comparing the radially averaged profiles in Figs. 3(j) and 3(k). However, it can be counteracted by assigning larger disks to the lower-k lattice, which enhances scattering into low in-plane momentum regions. As shown in Fig. 3(l), manipulation of the resonators' dimensions enables tuning the relative intensities of the inner and outer rings, which cannot be achieved through momentum-space addition. A detailed analysis of the nano-resonator geometry's effect on the relative scattering intensities is beyond the scope of this work and will be tackled in the future.

In summary, we demonstrate that the real-space addition of two metasurfaces enables the reproduction of superimposed angular features. The relative scattering intensity can be tuned by adjusting the size of the decoration unit, providing an easy way to control scattering over different angular ranges. Although this concept is powerful, it is inherently limited by geometrical upper limits on the density of points needed to achieve angular scattering in various regions and on the maximum size of decoration units. Furthermore, the non-interacting assumption for the two metasurfaces is expected to break down when the distance between nano-scatterers decreases. Future work is needed to explore the limits of such interactions between two or more superimposed metasurfaces and to develop design guidelines for potential applications.

3.4 Defining the Spectral Response by Choice of Decoration Unit

In our design framework, we assume that the spatial arrangement of the decoration units governs the angular scattering response. However, each decorator simultaneously acts as an individual resonator, allowing for precise spectral control.[42,43] To investigate the spectral tunability, we conduct a simulation study of dielectric, lossless resonators, complementary to the experimental part. In particular, we compare differently shaped dielectric resonators placed at identical positions (i.e., the metasurfaces are created from the same point pattern) on a lossless, dispersion-less dielectric substrate. In these simulations, we use a lossless dielectric with constant refractive index ($n = 3.5$) to isolate geometry-induced effects on the scattering response of the metasurface without the effects of material absorption. As a reference, we also include a pattern generated by thresholding the same GRF image (see Sec. 2 for more details) to isolate the influence of the resonator shape. As shown in Fig. 4(a), we evaluate four configurations, from left to right: a thresholded GRF pattern (black), a point pattern decorated with solid disks ($r = 100$ nm, green), four-point star-shaped structures ($r_{\text{tip}} = 64$ nm, $r_{\text{indent}} = 155$ nm, purple), and rings ($r_{\text{inner}} = 75$ nm, $r_{\text{outer}} = 125$ nm, orange). The chosen shapes are selected to exhibit distinct resonant spectra while maintaining a consistent filling fraction of ~16% to ensure a fair comparison by isolating the effects of the structural arrangement from those of material coverage. The SDFs of all four 2D patterns are very similar [see Fig. 4(b)], indicating that the form factor of the resonators has minimal effect on the spatial frequency distributions. Notably, the SDFs of the four-point star and disk patterns are nearly identical, whereas that of the ring pattern shows a slight deviation due to the ring's form factor. Given the similar SDFs and comparable filling fraction among the patterns, differences in the scattering spectra can be solely attributed to the nano-resonator. To study the angular and spectral dependence of scattering through the patterns, we calculate the far-field forward scattering for each pattern implemented as 200 nm-high resonators made of a dielectric of $n = 3.5$ on a semi-infinite lossless substrate using FDTD simulations. Figure 4(c) shows the calculated scattered power fraction as a function of photon energy and in-plane momentum ($k_{//}$). The targeted angular scattering region given by the SDF is highlighted with dotted white lines. In all patterns, the scattered power is concentrated within this region. However, the scattering intensity within the $k \in [10, 20]$ μm^{-1} interval exhibits strong dependence on the photon energy, where the trend varies for the different resonator geometries. For the thresholded pattern, the scattered power fractions show a broadband feature centered at ~1.7 eV. The scattering from the decorated metasurfaces displays two distinct scattering peaks, with energies that blue-shift as they move from the disks to the ring resonators. The spectral dependence is better quantified by integrating the scattered power over the $k \in [10, 20]$ μm^{-1} interval [Fig. 4(d)].

The integrated power fractions show that, depending on the incident photon energy, more than 50% of the incident power can be scattered into the designed angular range. By comparing the integrated power fractions with the forward scattering cross-sections of individual nano-resonators [Fig. 4(e)], we show that the spectral modulation originates from the excitation of resonant features that favor forward scattering. The origin of these is further discussed in the Supplementary Material. It appears that electric and magnetic dipole resonances dominate the scattering behavior, as expected from dielectric nano-resonators on substrates.[19] Adjusting the geometrical dimensions shifts the spectral position of the excitation, resulting in a design parameter that allows tuning the ensemble's response. We suspect slight spectra; differences are likely due to lattice interactions.[43,44]

3.5 Simultaneous Control over Spectral and Angular Scattering Response Using Real-Space Addition

Finally, we leverage the two distinctive features of our pattern generation approach to exploit its potential fully: on one hand, the possibility to decorate each position with a different scattering unit, and on the other hand, the flexibility to superimpose multiple point distributions in real space. Designing a metasurface in this way enables simultaneous and independent control over the angular and spectral scattering responses.

As a proof of concept, we target two different angular regions centered at $k_1 = 7.5$ μm^{-1} and $k_2 = 17.5$ μm^{-1} in a computational analysis. For this, we generate two point distributions with our approach using a triangular input function with a width of 5 μm^{-1}. Each point distribution is decorated with a different shape: one with a ring and one with a disk [Fig. 5(a)]. In Fig. 5(b), the corresponding SDFs are shown: blue for the sub-pattern with disk-shaped decoration units, which has features at higher angular frequencies; red for the sub-pattern with ring-shaped decoration units and features at lower angular frequencies; and gray for the real-space addition of the blue and red sub-patterns. As expected, the summation of the two patterns retains the angular features of the two sub-patterns: the SDF (gray line) of the addition-pattern shows features at the same positions as the sub-patterns creating it (blue, red lines).

Next, we simulate the angular and spectral scattering of a metasurface with this pattern consisting of a dielectric ($n = 3.5$, $h = 200$ nm) on a substrate of the same material with FDTD. It is evident from Fig. 5(c) that the angular scattering is enhanced in the designed ranges (vertical dashed lines). In each interval, at higher or lower in-plane momentum ranges, the scattering intensities peak at different photon energies. Integrating the power scattered into the targeted k-space regions [Fig. 5(e)] reveals enhanced scattering at spectral positions that correspond to the forward scattering of the single nano-resonator. Here, the spectral scattering response is again clearly linked to the forward scattering of the resonator unit cell, likely stemming from exciting resonant behavior. This result highlights the versatility of our approach to tailoring the design of metasurfaces to specific applications by carefully adjusting the angular and spectral response.

4 Conclusion

In this work, we have introduced a non-iterative reverse design approach for correlated-disordered metasurfaces that allows simultaneously controlling the spectral and angular scattering of incident light. It is based on a 1D representation of the Fourier space, the SDF, and uses blob detection to identify correlated-disordered points with given angular scattering properties. A subsequent re-decoration step allows for further tailoring of the optical response. We fabricated the patterns as Au nano-pillars on Si substrates and used Fourier microscopy to measure the angular scattering of simple pillar distributions. The experimental results strongly support our claim that our binary pattern generation approach can be used to design metasurfaces with defined scattering properties. One key advantage of our proposed approach is the possibility of superimposing two metasurfaces via real-space addition. In a complementary computational analysis based on FDTD calculations of dielectric resonators, we show that the forward scattering properties of the single decoration unit modulate the ensemble's spectral scattering response, yielding a design parameter that can be tailored exclusively to the spectral range of interest. This feature allows us to design angular and spectral responses for specific applications independently.

Our straightforward method for designing metasurfaces does not rely on iterations, optimizations, or resource-intensive machine learning techniques, and we demonstrate how their angular and spectral characteristics of light scattering can be individually controlled. Although we acknowledge that implementing iterative optimization steps could further enhance the control over the angular scattering response, our method already provides flexible control over the point distribution. Moreover, we note that the available computational memory limits the lateral dimension of the metasurface design, so incorporating parallelization of the GRF generation and blob readout can allow one to design large-scale metasurfaces (~mm lateral size) with nm features. To highlight the advantages of our method's re-decoration strategy, we tune the spectral response by changing the resonator's geometry; however, the same concept can be extended to other properties, such as phase or polarization. All combined, we present a versatile toolbox for wavelength- and angle-selective metasurface engineering.

Our findings have implications for designing metasurfaces for potential applications such as light trapping in thin film photovoltaics, tailored lighting, or sensing, in which these capabilities are highly desirable. By targeting different angles at various spectral regions, light trapping in thin-film solar cells made from highly dispersive materials can be improved, thereby opening up pathways for the exploration of photovoltaic materials.[9] In tailored lighting or sensing applications, independent responses at different angles enable multiplexing, i.e., parallelizing different tasks or incorporating multiple reactions in a single device.[45,46] However, the fraction of power scattered to higher angles depends on the forward scattering cross-section of an individual resonator. This is a double-edged sword: although designing a nano-resonator with high forward scattering is theoretically possible, it may not be realistic for the chosen application in terms of geometrical parameters or materials. Moreover, targeting different angles at different wavelengths depends on superpositioning two independent, non-interacting metasurfaces in real space, which has inherent limitations, such as the point density of the two lattices limiting the geometry of potential decorators, and can lead to efficiency trade-offs. Therefore, further studies should establish design guidelines, explore the limitations of such metasurfaces, and benchmark their performance against established ones in potential applications.

Disclosures

While preparing this work, the authors used ChatGPT to refine the code and Grammarly to edit the language. The authors reviewed and edited the content as needed and take full responsibility for the publication's content.

Code and Data Availability

The data supporting the findings of this study, including the design workflow, experimental measurements, and simulation outputs, are publicly available at https://doi.org/10.5281/zenodo.20048441.

Acknowledgments

This project has received funding from the European Union's Horizon 2020 research and innovation programme under the Marie Skłodowska-Curie grant agreement (Grant No. 945363). The authors thank the EPFL Center for Imaging for the helpful discussions and EPFL CMi and CiMe for the nano-fabrication and characterization infrastructure. This work is part of the Dutch Research Council (NWO) and was partly performed at the research institutes AMOLF and ARCNL. The Advanced Research Center for Nanolithography ARCNL is a public–private partnership among the University of Amsterdam, Vrije Universiteit Amsterdam, University of Groningen, the Netherlands Organization for Scientific Research (NWO), and the semiconductor equipment manufacturer ASML. This work used the Dutch national supercomputer Snellius with the support of the SURF Cooperative (Grant Nos. EINF-8457 and EINF-9404).

References

1. V. Neder et al., "Combined metagratings for efficient broad-angle scattering metasurface," *ACS Photonics* **6**, 1010–1017 (2019).
2. M. Haghtalab et al., "Ultrahigh angular selectivity of disorder-engineered metasurfaces," *ACS Photonics* **7**, 991–1000 (2020).
3. I. Koirala, S.-S. Lee, and D.-Y. Choi, "Highly transmissive subtractive color filters based on an all-dielectric metasurface incorporating TiO_2 nanopillars," *Opt. Express* **26**, 18320–18330 (2018).
4. N. Yu and F. Capasso, "Flat optics with designer metasurfaces," *Nat. Mater.* **13**, 139–150 (2014).
5. J. Balthasar Mueller et al., "Metasurface polarization optics: independent phase control of arbitrary orthogonal states of polarization," *Phys. Rev. Lett.* **118**, 113901 (2017).
6. A. Arbabi et al., "Dielectric metasurfaces for complete control of phase and polarization with subwavelength spatial resolution and high transmission," *Nat. Nanotechnol.* **10**, 937–943 (2015).
7. E. B. Whiting et al., "Meta-atom library generation via an efficient multi-objective shape optimization method," *Opt. Express* **28**, 24229–24242 (2020).
8. T. Liu et al., "Multipole and multimode engineering in Mie resonance-based metastructures," *Nanophotonics* **9**, 1115–1137 (2020).
9. N. Tavakoli et al., "Over 65% sunlight absorption in a 1 μm Si slab with hyperuniform texture," *ACS Photonics* **9**, 1206–1217 (2022).
10. M.-C. van Lare and A. Polman, "Optimized scattering power spectral density of photovoltaic light-trapping patterns," *ACS Photonics* **2**, 822–831 (2015).
11. S. Yu et al., "Design of non-deterministic quasi-random nanophotonic structures using Fourier space representations," *Sci. Rep.* **7**, 3752 (2017).
12. W.-K. Lee et al., "Concurrent design of quasi-random photonic nanostructures," *Proc. Natl. Acad. Sci. U. S. A.* **114**, 8734–8739 (2017).
13. J. Buencuerpo et al., "Engineering the reciprocal space for ultrathin GaAs solar cells," *Opt. Laser Technol.* **142**, 107224 (2021).
14. E. R. Martins et al., "Deterministic quasi-random nanostructures for photon control," *Nat. Commun.* **4**, 2665 (2013).
15. W. Ji et al., "Recent advances in metasurface design and quantum optics applications with machine learning, physics-informed neural networks, and topology optimization methods," *Light Sci. Appl.* **12**, 169 (2023).
16. S. Molesky et al., "Inverse design in nanophotonics," *Nat. Photonics* **12**, 659–670 (2018).
17. D. Chen and S. Torquato, "Designing disordered hyperuniform two-phase materials with novel physical properties," *Acta Mater.* **142**, 152–161 (2018).
18. J. Buencuerpo et al., "Efficient light-trapping in ultrathin GaAs solar cells using quasi-random photonic crystals," *Nano Energy* **96**, 107080 (2022).
19. J. Van De Groep and A. Polman, "Designing dielectric resonators on substrates: combining magnetic and electric resonances," *Opt. Express* **21**, 26285–26302 (2013).
20. N. A. Butakov and J. A. Schuller, "Designing multipolar resonances in dielectric metamaterials," *Sci. Rep.* **6**, 38487 (2016).
21. B. S. Luk'yanchuk et al., "Optimum forward light scattering by spherical and spheroidal dielectric nanoparticles with high refractive index," *ACS Photonics* **2**, 993–999 (2015).
22. A. Rahimzadegan et al., "A comprehensive multipolar theory for periodic metasurfaces," *Adv. Opt. Mater.* **10**, 2102059 (2022).
23. P. Spinelli and A. Polman, "Light trapping in thin crystalline Si solar cells using surface Mie scatterers," *IEEE J. Photovoltaics* **4**, 554–559 (2014).

24. N. Lee et al., "Multi-resonant Mie resonator arrays for broadband light trapping in ultrathin c-Si solar cells," *Adv. Mater.* **35**, 2210941 (2023).
25. L. S. Froufe-Pérez et al., "Role of short-range order and hyperuniformity in the formation of band gaps in disordered photonic materials," *Phys. Rev. Lett.* **117**, 053902 (2016).
26. S. Yu et al., "Characterization and design of functional quasi-random nanostructured materials using spectral density function," *J. Mech. Des.* **139**, 071401 (2017).
27. A. Iyer et al., "Designing anisotropic microstructures with spectral density function," *Comput. Mater. Sci.* **179**, 109559 (2020).
28. W. Shi, Y. Jiao, and S. Torquato, "Three-dimensional construction of hyperuniform, nonhyperuniform, and antihyperuniform disordered heterogeneous materials and their transport properties via spectral density functions," *Phys. Rev. E* **111**, 035310 (2025).
29. M. Teubner, "Level surfaces of gaussian random fields and microemulsions," *Europhys. Lett.* **14**, 403–408 (1991).
30. Z. Ma and S. Torquato, "Random scalar fields and hyperuniformity," *J. Appl. Phys.* **121**, 244904 (2017).
31. J. J. Koenderink, "The structure of images," *Biol. Cybern.* **50**, 363–370 (1984).
32. T. Lindeberg, *Scale-Space Theory in Computer Vision*, Springer US, Boston, Massachusetts (1994).
33. V. Majanga and S. Viriri, "Automatic blob detection for dental caries," *Appl. Sci.* **11**, 9232 (2021).
34. C. Di Ruberto, A. Loddo, and G. Puglisi, "Blob detection and deep learning for leukemic blood image analysis," *Appl. Sci.* **10**, 1176 (2020).
35. R. Manzorro et al., "Exploring blob detection to determine atomic column positions and intensities in time-resolved TEM images with ultra-low signal-to-noise," *Microsc. Microanal.* **28**, 1917–1930 (2022).
36. S. Van Der Walt et al., "scikit-image: image processing in Python," *PeerJ* **2**, e453 (2014).
37. S. Cueff, L. Berguiga, and H. S. Nguyen, "Fourier imaging for nanophotonics," *Nanophotonics* **13**, 841–858 (2024).
38. I. Sersic, C. Tuambilangana, and A. F. Koenderink, "Fourier microscopy of single plasmonic scatterers," *New J. Phys.* **13**, 083019 (2011).
39. C. I. Osorio, A. Mohtashami, and A. F. Koenderink, "K-space polarimetry of bullseye plasmon antennas," *Sci. Rep.* **5**, 9966 (2015).
40. A. Mohtashami, C. I. Osorio, and A. F. Koenderink, "Angle-resolved polarimetry of antenna-mediated fluorescence," *Phys. Rev. Appl.* **4**, 054014 (2015).
41. https://www.ansys.com/products/optics/fdtd.
42. K. Vilayphone et al., "Design rules for structural colors in all-dielectric metasurfaces: from individual resonators to collective resonances and color multiplexing," *ACS Photonics* **11**, 470–483 (2024).
43. V. E. Babicheva and A. B. Evlyukhin, "Multipole lattice effects in high refractive index metasurfaces," *J. Appl. Phys.* **129**, 040902 (2021).
44. V. I. Zakomirnyi et al., "Collective lattice resonances in disordered and quasi-random all-dielectric metasurfaces," *J. Opt. Soc. Am. B* **36**, E21–E29 (2019).
45. P. P. Iyer et al., "Unidirectional luminescence from InGaN/GaN quantum-well metasurfaces," *Nat. Photonics* **14**, 543–548 (2020).
46. J. Liu and R. Paiella, "Gradient-metasurface directional photodetectors," *Opt. Lett.* **49**, 1417–1420 (2024).

Anja Tiede is a researcher at the interface of photonics and materials science, focusing on correlated-disordered nanophotonic structures for controlling light-matter interactions. Her work combines optical simulation, semiconductor nanofabrication, and device engineering. She obtained her PhD from École Polytechnique Fédérale de Lausanne in 2026 and was supported as an EPFLglobaLeaders fellow through the Marie Skłodowska-Curie Actions program

Esther Alarcon-Llado is a professor at the University of Amsterdam and group leader at the NWO-Institute AMOLF, where she leads the 3DPhotovoltaics group since 2016. She received her PhD in Physics from the University of Barcelona. Before joining AMOLF, she was a postdoctoral fellow at a*STAR IMRE, Lawrence Berkeley National Laboratory and École Polytechnique Fédérale de Lausanne. Her group's research brings together nanophotonics, nano-electrochemistry, and scanning probe microscopy.

Biographies of the other authors are not available.